FULL PAPER

ADVANCED
OPTICAL
MATERIALS

www.advopticalmat.d

Check for
updates

2D Allotrope of Carbon for Self-Powered, Flexible, and Transparent Optoelectronics

Yujie Guo, Luhong Zhang, Dan Jin, Yangfan Lu, Zhenyu Xu, Jinchun Jiang, Ziyu Yang, Huawei Liang, Hui Fang,* Shuangchen Ruan, and Yu-Jia Zeng*

Flexible and transparent optoelectronics based on 2D materials are promising candidates for next-generation technologies. Among all 2D materials, it is of numerous practical implications to explore nonmetal, earth-abundant candidates. Herein, an exciting addition is unearthed—2D hydrogenized amorphous carbon (α-C:H). The 2D α-C:H nanosheets, with layered structural feature, are composed of crystalline sp^2 nanoclusters embedded in sp^3 amorphous matrix. The typical "vapor–solid" mechanism governs the growth of these nanosheets under the temperature–pressure combination above the Berman–Simon line. Their high transmittance over 97.7% covers the 425–1300 nm wavelength region. Optical characterizations also reveal a spectral overlap between the π–π^* absorption edge and σ–σ^* photoluminescence peak. Self-powered and flexible photodetectors based on the 2D α-C:H/ZnO heterostructure exhibit a remarkable photoresponse, with a broadened photosensitivity responsivity of 195.16 mA W^{-1} and a 267-fold decrease of the rise time. This performance enhancement originates from the type II band alignment, the pyroelectric and piezo-phototronic effects. As a new member in the 2D family, α-C:H nanosheets promise to be appealing in transparent flexible optoelectronics with ultralow power consumption and real-time, on-site response.

1. Introduction

The new era of the Internet of Things (IoT) has spawned the urge of transparent and flexible devices.[1–3] In the IoT sensor network, critical demands are aroused for the flexible optoelectronics to monitor, image, and communicate the correlated physical objects.[4,5] The initial premise is the mechanical flexibility that makes the devices adaptable and sustainable to arbitrary surface topologies. In order to achieve lightweight and high portability, self-powered behavior is preferable as it does not require external power sources. The ultrasensitive and ultrafast signal detection is also essential for dynamic and real-time data collection. In an attempt to meet all the above requests, significant efforts have been devoted to the incorporation of 2D materials in next-generation optoelectronics. So far, 2D materials have established themselves as an intriguing building block in photodetectors owing to their distinctive properties including strong light–matter interaction and superior carrier mobility.[6,7] The atomic-level thickness underpins their substantially high transmittance and durability against bending.[8,9] Further performance modulation and optimization can be realized by the heterogeneous integration beyond the restriction of lattice matching owing to their dangling bonds' free nature.

Among all emerging 2D materials, graphene remains at the center of ever-expanding research areas due to its room-temperature ballistic transport, functional versatility, and high chemical stability.[9,10] Along with graphene, the need for 2D materials composed of nonmetal and earth-abundant elements is more eminent, as the contrary based on transition metals are restricted by the limited availability and recycling rate. To date, the most prevalent nonmetal, light-element based 2D material phosphorene has not yet conquered its poor stability issue.[11–13] The other members, including h-BN, BCN, fluorographene, graphene oxide, and graphitic carbon nitride (g-C$_3$N$_4$), have reached a level of competitiveness in the postsilicon era.[14,15] Yet, the widely spread search of the 2D allotropic form of carbon has been spawned from the perspective of compositional compatibility, manufacturing simplification, and device miniaturization. Nevertheless, albeit with the great variety of carbon hybridizations and thereby bulk C allotropes, the exploration of the 2D counterparts stays mostly theoretically, enumerated to be graphyne, pentagraphene, tetrahexcarbon, pentahexoctite, and T-graphene.[16–19] Apart from graphene, the only 2D mesostructure carbon experimentally obtained is

Dr. Y. Guo, Dr. L. Zhang, Z. Xu, Dr. J. Jiang, Dr. Z. Yang, Prof. H. Liang,
Prof. S. Ruan, Prof. Y.-J. Zeng
College of Physics and Optoelectronic Engineering
Shenzhen University
Shenzhen 518060, P. R. China
E-mail: yjzeng@szu.edu.cn
D. Jin, Prof. H. Fang
Institute of Microscale Optoelectronics
Nanophotonics Research Center
Shenzhen University
Shenzhen 518060, P. R. China
E-mail: fhui79@szu.edu.cn
Dr. Y. Lu
School of Materials Science and Engineering
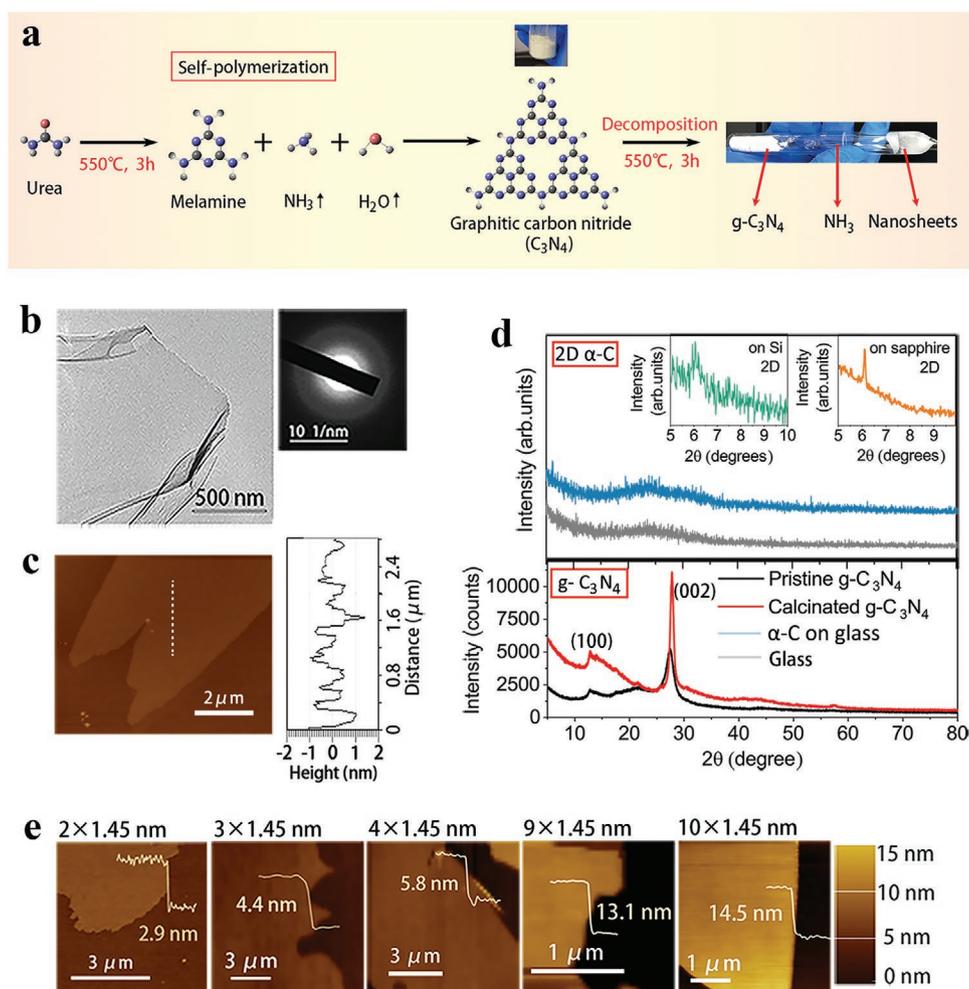Zhejiang University
Hangzhou 310027, P. R. China

self-assembled instead of being a continuous nanosheet with a layered structural feature.[18]

Herein, we report on an exciting addition to the 2D allotrope of carbon—2D α-C:H nanosheets. They are synthesized via a cost-effective route that avoids the huge facility investment involved in the growth of conventional α-C films.[19] The nanosheets possess intriguing morphology of large-scale, ultrasmooth surface, and high structural homogeneity. Throughout self-consistent chemical analyses, the layered structural nature of these nanosheets is investigated, stacking with α-C embedded with crystalline sp^2 nanoclusters. Their formation follows the typical "vapor–solid" (V–S) mechanism under the temperature-–pressure combination above the Berman–Simon line. Then, comprehensive optical characterizations unravel the high transmittance comparable to monolayer graphene over a visible–IR wavelength region of 425–1300 nm. A broad spectral overlap in the absorption and photoluminescence (PL) spectra is also detected, owing to the co-existed π–π^* and σ–σ^* bandgaps. Given all these superior properties of 2D α-C:H, self-powered flexible photodetectors are fabricated by incorporation of the nanosheets with the ZnO film, one of the most extensively investigated semiconductors used in UV photodetectors owing to its wide bandgap (3.37 eV), high room-temperature exciton binding energy (60 meV), and earth-abundant, nontoxic characters.[20] Remarkable photoresponse has been achieved, especially an extended photoresponse range, a high responsivity of 195.16 mA W^{-1}, and 267-fold rise-time shortening. The fundamentals of these performance enhancements are congruously derived from the type II heterogeneous integration, the piezo-phototronic effect, and the pyroelectric effect. Our study has blossomed the 2D α-C:H nanosheets into a promising material for the bidirectional optical signal transmission and transparent flexible optoelectronics with ultrahigh power efficiency.

2. Results and Discussion

Figure 1a schematically illustrates the two-step synthesis protocol of the emerging nanosheets. Using urea as the
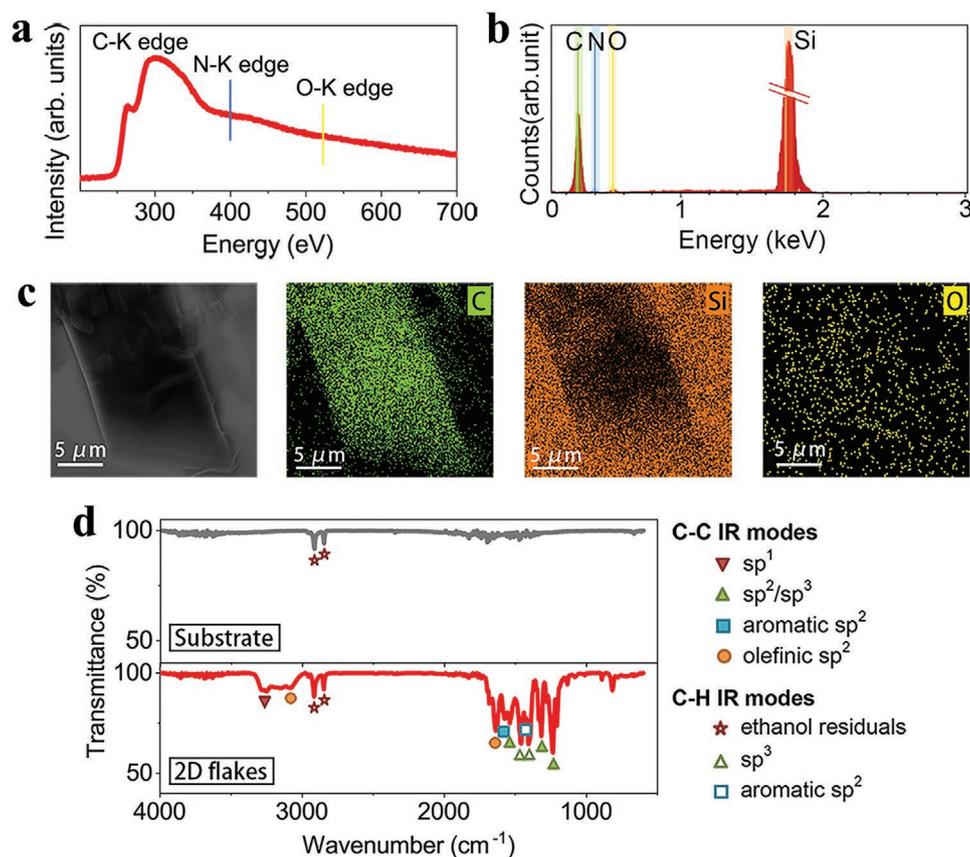

Figure 1. a) Two-step synthesis route of the nanosheets. b) TEM image of a nanosheet and the corresponding SAED pattern. c) Left: AFM image of a nanosheet; right: the profile of the RMS roughness measured plotted along the dashed line in the AFM image. d) Top: XRD patterns of the nanosheets spread on the glass substrate and the reference glass substrate; inset: XRD patterns of the nanosheets dispersed on the Si and sapphire substrates; bottom: XRD patterns of the pristine and calcinated g-C$_3$N$_4$ powders. e) AFM images of nanosheets of the thickness with 2, 3, 4, 9, and 10 times of 1.45 nm.

precursor, g-C$_3$N$_4$ powders were initially fabricated via the self-polymerization reaction, in which melamine and ammonia gas worked as the intermediates. These powders then underwent a thermal treatment in a sealed tube at 550 °C for 3 h. At the end of the tube far away from the pristine powders, the deposited nanosheets were strongly adhesive to the tube inner wall. After dispersed in ethanol (Figure S1, Supporting Information), these nanosheets sustained the chemical stability for over a year, even after spreading on a variety of substrates (such as Si, glass, sapphire, and the transmission electron microscopy (TEM) grid). As indicated in the TEM images in Figure 1b and in Figure S1, Supporting Information, the nanosheets are highly continuous and crack free even when highly shrunk, highlighting their structural homogeneity and flexibility. The translucent appearance implies their ultrathin thickness. The lateral dimension of the nanosheets reaches over 100 μm, as shown in Figure S1 (Supporting Information). The ultrasmooth surface of the nanosheets is revealed by the root-mean-square (RMS) roughness of 1.04 nm derived from an atomic force microscope (AFM, Figure 1c). These morphological properties endow the nanosheets with high potential in transparent and flexible device applications. The strong diffuse scattering in the selected area electron diffractogram (SAED, inset of Figure 1b) indicates the amorphous status of the nanosheets. This is supported by the X-ray diffraction (XRD) pattern of the nanosheets dispersed on the glass substrate (Figure 1d), with

the absence of eminent peaks from the lattice plane reflection. Another notable feature of this spectrum is the emerging tiny peak at $2\theta = 6.1°$, which is also evident when spread on the Si substrate, and more pronounced on the sapphire (the inset of **Figure 2**b). This scenario implies the weak interlayer diffraction corresponding to a periodic spacing of 1.45 nm. It is interesting that the nanosheet thicknesses extracted from the AFM characterization are always a multiple of 1.45 nm, as exampled in Figure 1e. Furthermore, the most widely detected thickness of the large-scale nanosheets is ≈2.9 nm. These observations hint the layering feature of the nanosheets, which will be substantiated by the Raman spectroscopy in the following contexts.

Along with the formation of the 2D amorphous nanosheets, the pristine g-C$_3$N$_4$ powders go through a color evolution from yellow to white via calcination. As shown in Figure 1d, the XRD pattern of the calcinated powders presents more pronounced peaks at 13.1° and 27.3°, corresponding to the (100) and (002) reflections in g-C$_3$N$_4$. These results manifest the increased crystallinity of the powders after the thermal treatment. As probed by the X-ray photoelectron spectroscopy (XPS), the C/N atomic ratios of the powders are 78.44% and 76.99% before and after calcination, respectively, demonstrating minor perturbations from the theoretical g-C$_3$N$_4$ stoichiometry. Based on the law of mass conservation, a gaseous product—NH$_3$—is produced via the decomposition reaction along with g-C$_3$N$_4$ and 2D α-C, as discussed in detail in Figure S3 (Supporting Information).

Figure 2. a) K edge EELS spectrum of a nanosheet in the high-loss region of 200–700 nm. b) EDS spectrum of a rhomboid-shaped nanosheet on the Si substrate. c) SEM image of a nanosheet and the corresponding C, Si, and O EDS mappings. d) FTIR spectra of the nanosheets on Si and the reference Si substrates.
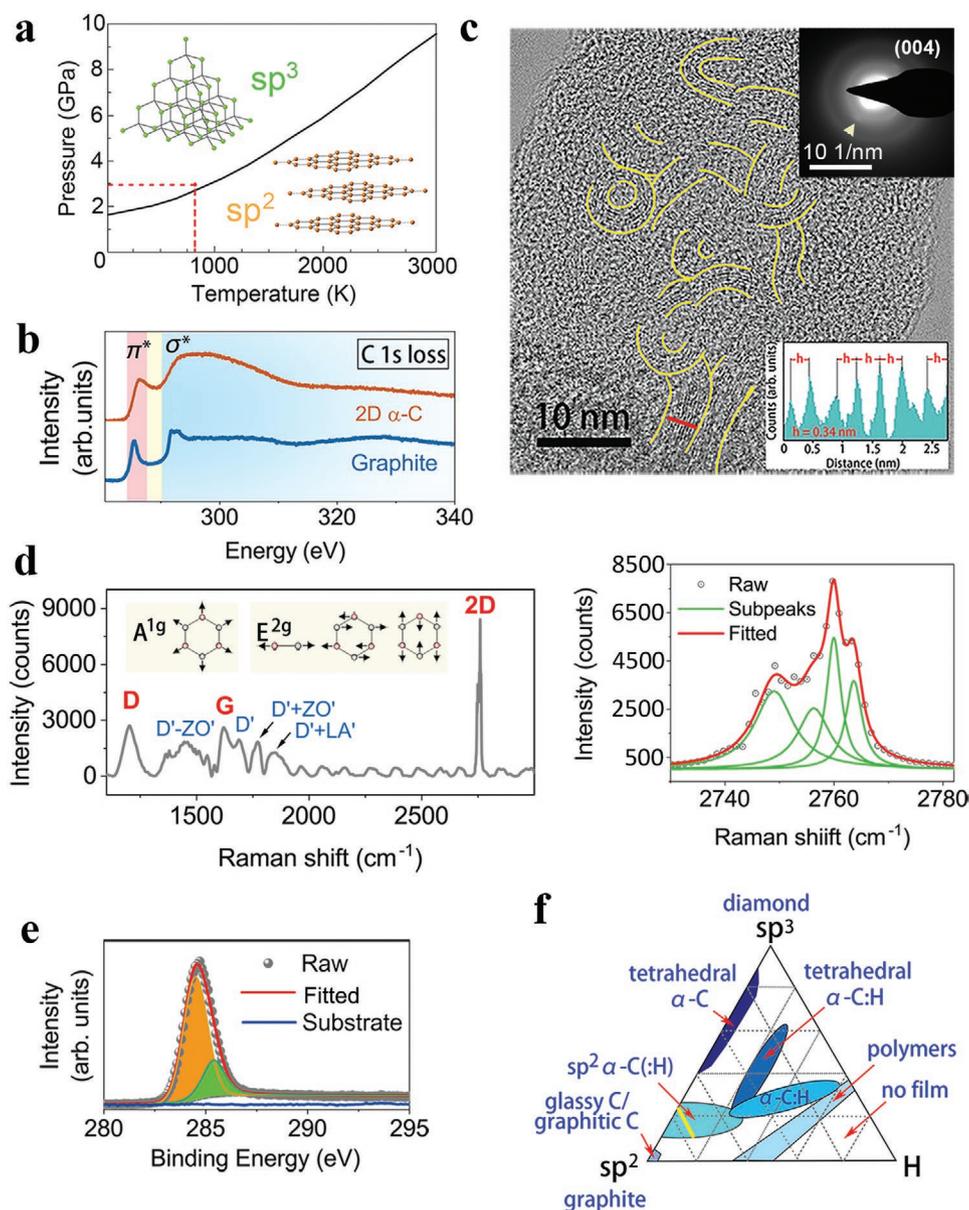
To study the nanosheets' composition, we conducted electron energy loss spectroscopy (EELS) measurements, with the resultant K edge spectrum in the high loss region from 200 to 700 eV presented in Figure 2a. The only detected peaks are ascribed to the C excitation, whereas the N and O ones are absent. This gives the solid evidence of the carbon composition of the nanosheets, which is in consistent with the pattern of energy dispersive spectrometry (EDS) measured from a rhomboid-shaped nanosheet deposited on the Si substrate (Figure 2b). To demonstrate the signal origins, a more intuitive compositional sketch is provided by the C, Si, and O EDS mappings in Figure 2c. The Si and C peaks derive predominantly from the substrate and the nanosheet, respectively, whereas the trace amount of O signals shows no distributional preference, stemming either from the ambient or the surface pollutants. The chemical bonds of the carbon allotrope are specified by a Fourier transform infrared spectrometer (FTIR). As shown in Figure 2d, all peaks refer to C—C modes and C—H bending modes in the nanosheets, apart from a few minor ones from the ethanol residues. These peaks, especially above 1340 cm^{-1}, are well localized.[19] This result unveils the nanosheets being composed of hydrogenated carbon (α-C:H). Particularly, the most profound C—H peaks are commonly associated with the sp^3 bonding, which can be explained by the saturation of dangling bonds via the ethanol passivation.[19] The diversity of C—C modes, especially those correlated with aromatic rings and olefinic bonds, implies the sp^2–sp^3 hybridized structure. To testify this structure, comprehensive analyses will be done in the following context.

To investigate the structure of the 2D α-C:H nanosheets, we initiate from the thermodynamic discussion based on the Berman–Simon phase diagram.[21] As depicted in **Figure 3**a, only when the combination of temperature and pressure surpasses the Berman–Simon line, the sp^3 bonding can be stabilized in the sp^2 structure. Inside the sealed tube during calcination at 823 K, the pressure gradually increases as the continuous release of NH_3. According to our estimation based on the ideal gas law (described in Section S3 of the Supporting Information), the system pressure peaks at 2.95 GPa, as indicated by the red dot in Figure 3a. Thereby, the circumstance in our system exceeds the minimal thermodynamic requirement for the hybridization of sp^2–sp^3 C network. This structural nature is verified by the EELS examination, as shown in Figure 3b. The C K edge spectrum consists of a peak centered at 285 eV and a step starting from 290 eV, which are derived from the excitation to π^* and σ^* states, respectively. The presence of the π^* peak distinguishes the nanosheets from the diamond, whereas, its σ^* step is of higher intensity than that of the reference graphite spectrum, demonstrating the richer sp^3 content in the nanosheet. Analogous results are obtained in the low-loss EELS spectrum in Figure S3 (Supporting Information). The probe of a scanning transmission electron microscope (STEM) provides a sketch of the π and σ sites' distribution. As shown in Figure 3c, small crystalline domains are randomly distributed in the disordered amorphous structure, as highlighted by yellow curves. The lattice spacing is extracted from the intensity profile plotted along the red line, which is perpendicular to the lattice fringes. The spacing of predominantly 3.4 Å is equivalent to the graphitic interlayer spacing, which is consistent with the

SAED pattern probed from the local crystalline domains (inset of Figure 3c). This short-term structural periodicity is also exampled in Figure S4 (Supporting Information), which elucidates the sp^2-bonded crystalline nanoclusters embedded in the sp^3 matrix. As indicated in the line profile, the lattice distances are occasionally enlarged owing to the local tension within the sp^2 sites induced by the cluster distortion. It is noteworthy that the nanosheet comprises no hexagonal lattice structure corresponding to the graphitic basal planes. This scenario indicates that the sp^2 clusters preferentially align vertically to the surface, which has also been observed in mobile sp^2 sites segregating into the graphitic clusters at elevated temperature.[19]

The C—C bonding of the 2D α-C:H nanosheets is further derived from the Raman spectroscopy, which is a technique ubiquitously utilized to characterize carbon materials.[22] As distinctive from graphene, the double resonance Raman spectroscopy can only be obtained under the excitation of the 660 nm laser.[23] When excited by the laser of shorter wavelengths, Raman signals are overshadowed by the PL ones. On the other hand, the 785 nm laser excitation only detects weak signals (Figure S4, Supporting Information), indicating the presence of a bandgap in 2D α-C:H. As identified in Figure 3d, the Raman spectrum presents the common "D" and "G" peaks of carbon materials, which are correlated with the A_{1g} breathing vibrations of rings, and the E_{2g} bond stretching of sp^2 atoms in both rings and chains, respectively.[23,24] Owing to the amorphous nature, both "D" and "G" peaks witness the defect-induced broadening and the dispersion of peak positions. To elaborate, the D peak intensity (I(D)) develops when the structural ordering in α-C elevates, as an opposite to graphene.[24] The relative intensity of the two peaks (I(D)/I(G)) varies inversely to the local grain size. Hence, the relatively profound D peak with I(D)/I(G) > 1 reveals the abundance of crystalline nanoclusters in the nanosheets. The shift of both peaks from their theoretical sites is in accordance with the reported Raman spectra of α-C under the 633 nm excitation,[25] manifesting the high structural disorder.[25,26] Particularly, the G peak dispersion is derived from the sp^2 clusters with narrower π–π^* bandgap.[27] Aside from these two peaks, several peaks are induced by the double resonance process, namely, the D'-ZO' (centered at 1465 cm^{-1}), D' (centered at 1695 cm^{-1}), D'+ ZO' (centered at 1775 cm^{-1}), D' + LA (centered at 1850 cm^{-1}), and 2D (centered at 2764 cm^{-1}) peaks.[24,28] Among them, the D' peak arises from the intravalley double resonance process; the D' + ZO' and D'−ZO' peaks are assigned to the Stokes and anti-Stokes combination of the E_{2g} longitudinal optical (LO) phonon and the B_{2g} out-of-plane (ZO') phonon layer-breathing modes, respectively; the D' + LA peak arises from the Stokes combination of the E_{2g} LO phonon and the transverse acoustic (TA) phonon branch; the 2D peak refers to the overtone of the D peak.[23] All of these phonon vibrational modes emerge owing to the local sp^2 nanocrystallization. Hence, the aforementioned spectroscopic analyses verify the nanosheets' structure with sp^2–sp^3 hybridization.

One of the most notable features of the Raman spectrum is the sharp 2D peak with ultrahigh intensity, which bears critical information on the layering nature of the nanosheets. Such a dominant intensity and sharpness of the 2D peak distinguish the nanosheets from the bulk α-C films. As enlarged in Figure 3d, the full-width at half-maximum (FWHM) of the
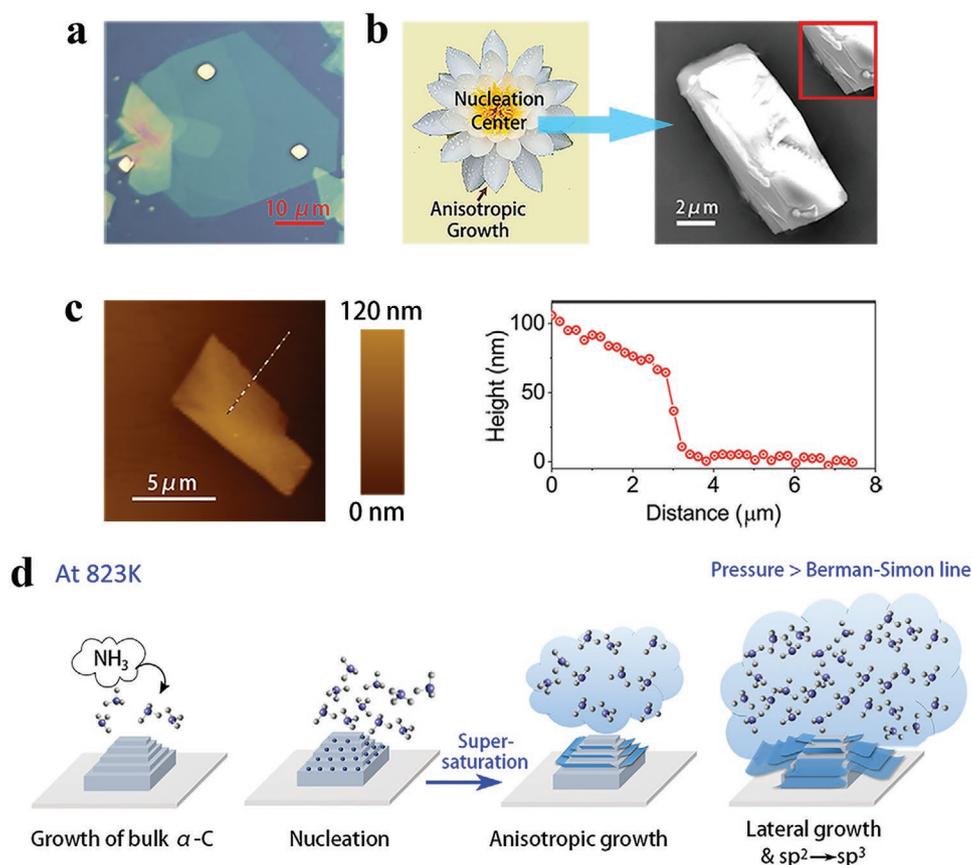
Figure 3. a) A schematic of the Berman–Simon phase diagram, in which the maximal system pressure at 823 K is marked by the red dot. b) C K edge EELS spectra of the nanosheet and the reference graphite. c) STEM image of a nanosheet, in which the crystalline nanoclusters are highlighted by yellow curves; inset: the intensity line profile plotted along the red line in the STEM image. d) Left: Raman spectrum of the nanosheets under the excitation of 660 nm laser; inset: a schematic of Raman E_{2g} and A_{1g} active phonon modes in carbons; right: the enlarged 2D peak with the multiple Lorentzian fits of its four components. e) High-resolution C 1s XPS spectra of the nanosheets and the substrate. f) The ternary sp^2–sp^3–H phase diagram.

2D peak is ≈15 cm^{-1}, even smaller than the single-layer graphene (SLG) counterpart. The asymmetric peak shape is highly assembly to that of bilayer graphene measured at 633 nm.[24] This peak splitting arises from to the intravalley double resonances during the excitation and recombination of excitons as well as the electron–phonon scattering.[25,28] These four components of the peak are testified by the nice multiple Lorentzian fits shown in Figure 3d. This phenomenon echoes our AFM probe, which demonstrates that the vast majority of the nanosheets have the thickness doubling 1.45 nm. Moreover, the 2D peak loses its doublet frequency relation with respect

to the D peak, which can be explained by the existence of crystalline nanoclusters.[27] Therefore, the Raman spectroscopy provides convincing evidence for the 2D α-C structure of the nanosheets at a more sophisticated level.

The quantitative analysis of the sp^2/sp^3 proportion in the nanosheets is facilitated by the XPS characterization. Theoretically, the subpeaks at 284.5 and 285.4 eV are assigned to the sp^2 and sp^3 hybridized atoms, respectively.[28] As shown in Figure 3e, the peak obtained from the high-resolution C 1s scan is solely attributed to the 2D α-C:H nanosheets, given the substrate spectrum is signal free. After deconvolution of

**ADVANCED
SCIENCE NEWS**
www.advancedsciencenews.com
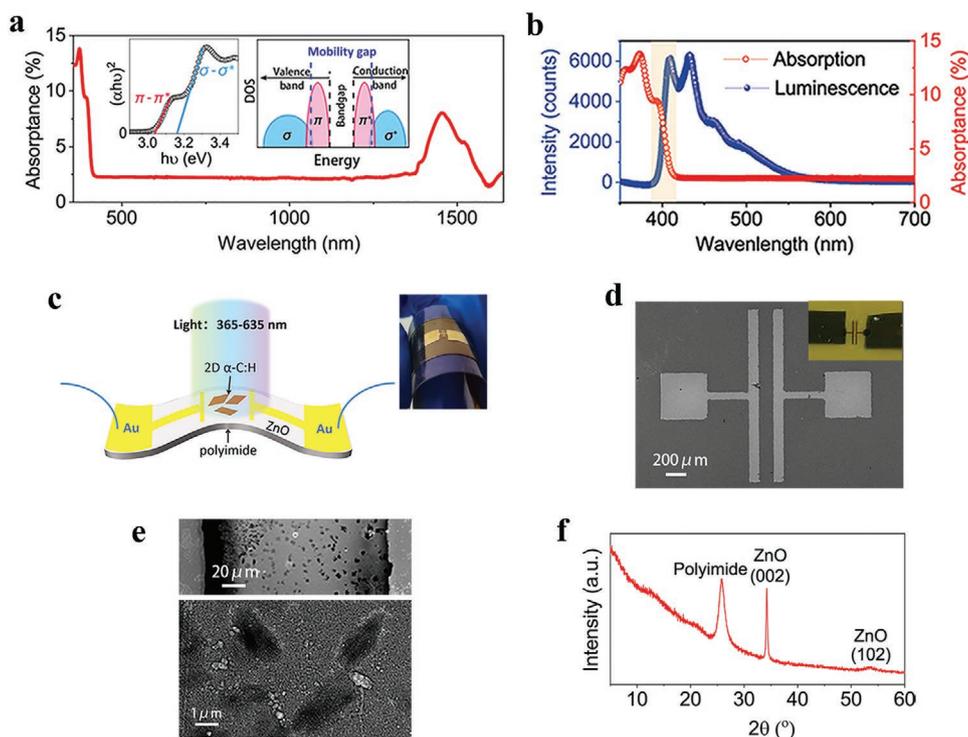
**ADVANCED
OPTICAL
MATERIALS**
www.advopticalmat.de

Figure 4. a) Optical microscope image of the typical petal-like arrangement of the as-grown nanosheets. b) SEM image of an isolated bulk center, in which an area of the terrace-like side is enlarged in the inset. c) Left: AFM image of a nucleation center; right: the height profile measured from the area marked by the dashed line. d) A scheme of the growth process of the 2D α-C nanosheets.

the spectrum, the average sp^3 content is derived to be 25.4%. As depicted in the ternary sp^2–sp^3–H phase diagram in Figure 3f, this sp^2/sp^3 proportion corresponds to the α-C(:H) phase, which is in consistent with our experimental deduction. Moreover, the estimated H content is below 15%, which is far away from the unstable polymeric region of high H content.[19] This composition makes the high stability of 2D α-C:H thermodynamically conceivable.

To unearth the formation mechanism of the 2D α-C:H nanosheets, we find that the as-grown nanosheets are always arranged in an exotic flower-like configuration. As shown in **Figure 4**a and in Figure S5 (Supporting Information), the nanosheets naturally stack like petals, rooting from a bulk carbon island. These islands are typically of lateral dimension less than 10 µm and thickness over 100 nm, as characterized by a scanning electron microscope (SEM) and AFM (Figure 4b,c). As indicated by the height profile extracted from AFM, the island possesses terrace-like sides with gradually decreased thickness toward the edges, from which the nanosheets grow laterally. Thereby, these islands, which compose of highly oxidized carbon based on our analysis in Figure S5 (Supporting Information), work as nucleation centers during the anisotropic growth of the homogeneous nanosheets. This phenomenon fulfils the typical characteristic of the V–S mechanism for the nanostructure growth.[29–31] As a consequence, with both

thermodynamic and kinetic discussions in mind, we sketch the growth process of 2D α-C:H nanosheets in Figure 4d. In the initial stage, the pristine g-C_3N_4 decomposes into vaporous C and NH_3 at the elevated temperature, which diffuses toward the other end of the tube owing to the concentration gradient. The vaporous C reaching the tube end first deposits into bulk C islands, in which the energetically active sites on the side terraces work as the nucleation centers. With continuously incorporation of C atoms, the supersaturation of the nucleation centers gives rise to the lateral growth of nanoflakes. Simultaneously, the persistent NH_3 release elevates the tube pressure. When the pressure exceeds the Berman–Simon line at 823 K, metastable sp^3 bonds start to build via the penetration of incident C atoms into the sp^2-bonded surface. As sp^3 bonds intrinsically increase the local density, the resultant local compressive stress ought to be relaxed to reach quasi-thermodynamic equilibrium. Given previous simulation, this relaxation is achieved by converting a few sp^3 bonds to π orbitals aligning vertically to the surface,[19] which agrees well with our experimental observations. As a consequence, these two synergetic yet competing procedures, confined-dimensional growth and sp^2–sp^3 mixture, have spawned the 2D α-C:H nanosheets.

Optical properties of the nanosheets, in terms of absorption and luminescence, are exploited. **Figure 5**a plots the ultraviolet–visible–near infrared (UV–vis–NIR) optical absorption spectrum

Figure 5. a) UV–vis–NIR optical absorption spectrum of the nanosheets' suspension; inset: Tauc's plot made under the direct bandgap hypothesis, and a schematic of the bandgap and mobility gap. b) PL spectrum of nanosheets in comparison with the absorption spectrum. c) A schematic of the flexible heterojunction-based photodetector and the corresponding photo. d) SEM image of the device channel deposited with the Au electrodes, inset: the corresponding optical microscope image. e) Top: a SEM image of the device channel, showing the ZnO film randomly spread with 2D α-C nanosheets; bottom: a zoom-in picture taken at the high magnification. f) XRD pattern of the ZnO film grown on the polyimide substrate.

of the 2D α-C:H nanosheets in the ethanol suspension. The transmittance exceeds 97.7%, comparable to the monolayer graphene, covering an ultrawide wavelength range from 425 to 1300 nm. This light transmission property endows 2D α-C:H nanosheets with a promising prospect in the application of transparent devices. There are double absorption edges below 420 nm, arising from the π–π* and σ–σ* excitations.[19] Based on the Tauc's plot under the direct bandgap hypothesis, the σ–σ* and π–π* bandgaps are derived to be 3.16 and 3.04 eV, respectively (inset of Figure 5a). The estimation of the direct bandgap condition is made due to the better fit and convergence than the indirect bandgap counterpart, as shown in Figure S6 (Supporting Information). The extracted bandgap energy exceeds the excitation energy for double resonance Raman measurements (1.88 eV), which can be explained by the highly localized π states within the σ–σ* gap. As schematically demonstrated in the inset of Figure 5a, the mobility gap of 2D α-C:H is much wider than its bandgap, as a typical characteristic of amorphous semiconductors.[19] This results in the strong localization of the C states in the π–π* bandgap and the band tails. The optical transitions are only allowed in extended–extended states,[19] whereas double resonance Raman scatterings can be triggered in the localized states. This strong localization of states also significantly hinders the carrier mobility in the nanosheets. In the NIR region between 1375 and 1595 nm, a second eminent absorption band is detected, in accordance with the FTIR observation (Figure 2d). This absorption covers the E, S, C, and L telecommunication bands that dominate the optical communication with low signal
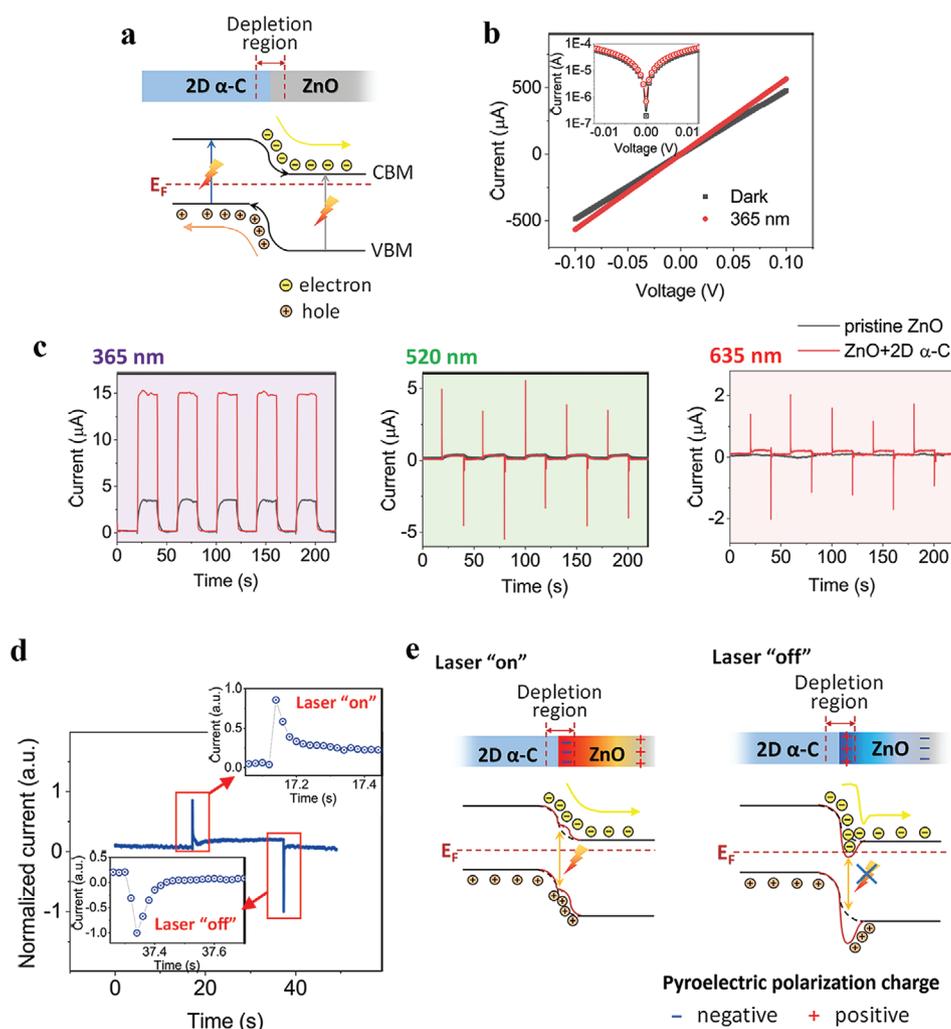
attenuation, making 2D α-C:H nanosheets intriguing for data communication, remote control, and radar systems.[31]

The PL spectrum of 2D α-C:H nanosheets spread on the glass substrate is showed in Figure 5b. Albeit with the nanosheets' amorphous nature, the spectrum presents strong and well-defined PL peaks. The radiative decay of optical excitons in α-C is attributed to the typical Forster tunneling mechanism, where the excitons hop among clusters and disordered networks via dipolar coupling.[19] Hence, the stepwise edges in the PL spectrum are associated with the diverse hopping possibilities inside the σ–σ* gap, the π–π* gap, and the band tails, respectively. When comparing the absorption and PL spectra, a small Stokes shift of ≈50 meV is observed. Noticeably, owing to the coexistence of the lower- and higher-energy bandgaps, the π–π* absorption edge overlaps with the σ–σ* PL peak, remaining high signal intensity within the spectral overlapping over 385–420 nm. Thereby, the nanosheets can be optically sensitive to the light emitted from themselves, which means, they are not only promising for separated applications in both the generation and reception of optical signals, but also capable of integrating these two capabilities into one device.[32]

The viability of light sensing in the 2D α-C:H nanosheets is evaluated. Nevertheless, their poor mobility, which originates from the high defect density and strong localization of C states within the mobility gap, prohibits the extraction of photogenerated carriers. To conquer this barrier, the 2D α-C:H nanosheets were coupled onto a ZnO film to form a heterostructure-based photodetector. In the devices, the ZnO film not

ADVANCED
SCIENCE NEWS
www.advancedsciencenews.com

ADVANCED
OPTICAL
MATERIALS
www.advopticalmat.de

only serves as a carrier–transport channel, but also facilitates the photon detection by band alignment at the heterointerface, as well as by its intrinsic piezoelectric effect arising from the non-centrosymmetric wurtzite structure. Figure 5c sketches the architecture of the flexible ZnO/2D α-C:H photodetector, along with a device photo. A ZnO film with the thickness of $\approx$200 nm was sputtered on a polyimide substrate, which was followed by the deposition of Au electrodes and dispersion of 2D α-C:H nanosheets. The configuration and dimension (150 μm × 2 mm) of the channel are demonstrated by the SEM and optical microscope images in Figure 5d. By taking a closer look at the channel, as shown in Figure 5e, the randomly distributed nanosheets are nicely attached to the ZnO surface. The ZnO film comprises numerous grains, implying its polycrystalline nature. The preferential c-axis-aligned crystallization with respect to the polyimide surface is verified by the XRD pattern shown in Figure 5f.

The photoresponse of the ZnO/2D α-C:H heterojunction was detected under the UV–vis irradiation, revealing a photosensitive band ranging from 365 to 635 nm. This band is evidently broadened than the pristine ZnO counterpart. Note that the pristine ZnO is only sensitive to the 365 and 520 nm illumination, owing to the band-to-band excitation and oxygen deficiencies, respectively.[33] Hence, the extension of the photosensitive band is believed to result from the heterogeneous integration. To elaborate, the nice incorporation between the 2D α-C:H nanosheets and the ZnO film is ensured by their morphological features, including a large-scale, high flexibility, ultrasmooth surface and high structural homogeneity. The well-defined heterointerface is subjected to the type II band alignment, as shown by the band diagram in **Figure 6**a. This alignment is deduced from two facts: i) ZnO and conventional α-C(:H) are naturally n-type and p-type, respectively;[19,34,35] ii) the type I (straddling gap) and type III (broken

Figure 6. Photoresponse with the assistance of the heterogeneous integration and pyroelectric effect. a) Type II band alignment at the interface between the ZnO film and the 2D α-C nanosheet. b) Current versus voltage (I–V) curves of the ZnO/2D α-C photodetector under the dark condition and the 365 nm light illumination; inset: log|I|–V curves in the small scale around the original point. c) Current versus time (I–t) curves of the devices detected under the zero external bias and illumination of 365, 520, and 635 nm lasers, respectively. d) The typical "four-stage" dynamic current fluctuation of the pyroelectric effect; insets: the I–t curves at the laser "on" and "off" moments, respectively. e) The band alignment at the ZnO/2D α-C interface triggering the pyroelectric process when turning on and off the laser.

ADVANCED
SCIENCE NEWS

www.advancedsciencenews.com
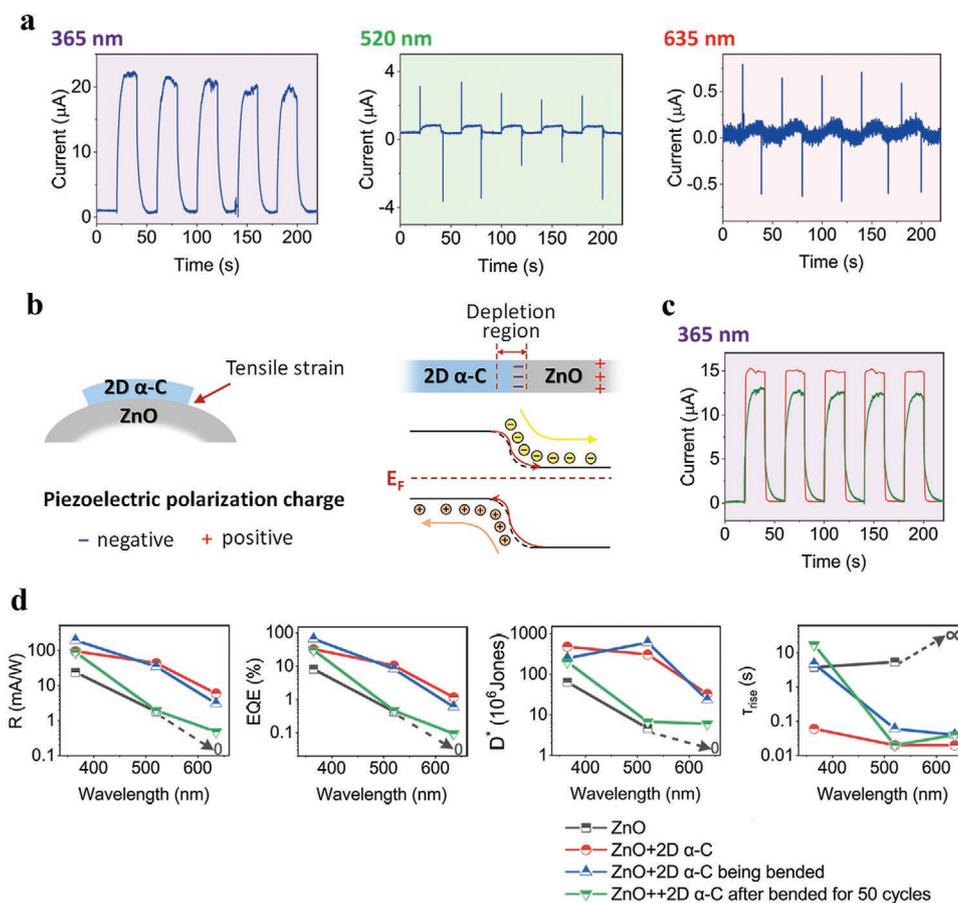
ADVANCED
OPTICAL
MATERIALS

www.advopticalmat.de

gap) alignments are precluded in our devices, as discussed in Figure S6 (Supporting Information). The interface staggering gap formed by the type II band alignment gives rise to a build-in potential, efficiently separating and migrating the photo-generated carriers even under the sub-band optical exposure.[36] As a verification, a rigid heterostructure-based photodetector is also fabricated, by coupling the 2D α-C:H nanosheets with the perfectly c-axis-aligned ZnO film on the sapphire substrate. As shown in Figure S6 (Supporting Information), the device is sensitive to lights with a wavelength up to 520 nm, whereas the commercial ZnO film only responses to the UV light owing to the low defect density. Consequently, we confirm that the extension of the photosensitive wavelength region of the heterojunction originates from the type II band alignment at the ZnO/2D α-C:H interface.

Figure 6b plots the current versus voltage (I–V) curves of the flexible ZnO/2D α-C:H photodetector in the presence and absence of the UV light illumination. Their nice linearity indicates the Ohmic contact between the channel and electrodes. Together with the enhanced I–V slope after the laser exposure, the phenomena unveil the photoconductive effect dominating the photoresponse. The photocurrent, which is defined as the current difference under the illuminated and dark conditions: $I_{ph} = I_{light} - I_{dark}$, substantially increases after the establishment of the heterostructure. For an intuitive interpretation, Figure 6c plots the time-resolved current (I–t) curves detected from the pristine ZnO and ZnO/2D α-C:H photodetectors under zero bias and 365–635 nm laser irradiations. The nice on/off repetition illustrates the high device reliability and durability to the optical exposure. After the formation of heterojunction, I_{dark}, in the magnitude of 10^{-7} Å, are slightly suppressed. This is ascribed to the consumption of a trace amount of majority carriers for the generation of the depletion region at the interface. On the other hand, the I_{light} enhancement is prominent, especially by a factor of ≈400% under the UV radiation. Similar to the extension of photosensitive band, the I_{light} elevation in the heterojunction is derived from the type II band alignment as well. Specifically shown in Figure 6a, after the photon absorption in both ZnO and 2D α-C:H, massive photoexcitons are generated. The staggering gap at the interface facilitates the generation, separation, and migration of oppositely charged photocarriers. As a result, excessive electrons are injected and accumulated within the ZnO channel. Finally, the internal potential imbalance at two electrodes drives the electrons, resulting in a drastically boosted I_{light} under zero bias.

Upon the stimuli of visible lights (520 and 635 nm), as presented in Figure 6b, semblable but less pronounced photocurrent enhancement is observed. Under these wavelengths, the photoresponse is dominantly optimized by the transient current fluctuation at the moment of turning "on" and "off" the lasers. When enlarged in Figure 6d, the dynamic current behavior typically follows four stages. At stage I, turning on the laser induces an instant current enhancement, which drops to a plateau within an extremely short duration (stage II). At the laser "off" moment, a transient current variation in the reversed direction is detected (stage III), recovering to I_{dark} immediately (stage IV). This process is representative in the pyroelectric effect. The underlying fundamental is the perturbation of spontaneous polarization in the ZnO film, which is induced

by the sudden thermal fluctuation of the heterostructure when switching on and off the laser.[37] As depicted in Figure 6e, when turning on the laser, a negative pyroelectric polarization potential (pyropotential) is generated at the ZnO/α-C:H interface, leading to an abrupt upward band bending. Hence, the electron accumulation is facilitated in the ZnO film and results in an instant current enhancement. Since the temperature rise induced by UV–vis laser radiance is transient, the pyropotential disappears soon enough, so that the photocurrent falls back to the equilibrium value. By virtue of the same mechanism, turning off the laser results in an abrupt downward band bending at the interface. This causes the local electron trapping within ZnO, and hence an instant current drop. The pyroelectric effect endows the heterostructure-based photodetector with a tremendous performance optimization, reaching the photocurrent increase by a factor of 24.28, as well as the maximal 267-fold decrease of the rise time (τ_{rise}).

To further modulate the performance of the self-powered ZnO/2D α-C:H photodetector, we induce the piezo-phototronic effect by imposing 0.45% strain to the channel, with the bending setup shown in Figure S7 (Supporting Information). I–t curves of this flexible device are presented in **Figure 7**a when subjected to zero external bias and UV–vis light illumination. Regardless of wavelengths, the photocurrent under the equilibrium status is congruously enhanced after bending, particularly a maximal 104.19% I_{ph} elevation under the 365 nm illumination. The underlying mechanism of this enhancement is the piezo-phototronic effect that can be schematically interpreted by the band diagram in Figure 7b. During bending, the tensile stress is imposed at the ZnO/2D α-C:H interface, while the compressive stress at the ZnO/polyimide interface. Owing to the tensile strain, negative piezoelectric polarization charges are generated at the ZnO/2D α-C:H interface. The piezoelectric polarization potential (piezopotential) may have two origins: one is from the non-centrosymmetric wurtzite ZnO structure, leading to the relative displacement of Zn^{2+} with respect to O^{2-} along the c-axis under the tensile strain.[38,39] Hence, the preferential c-axis alignment of the ZnO film (Figure 5f) is critical for triggering the piezoelectric effect. The other is from the heterointerface polar asymmetry, which is ubiquitous among heterostructures to trigger pyroelectricity and piezoelectricity.[40–45] The resulting piezopotential is maintained as long as the film is deformed, lending to the constant upward band bending at the interface, as shown in Figure 7b. Upon the light exposure, the photon-excited electrons are separated and migrate across the ZnO/2D α-C:H interface, leading to a substantially increased electron density within the ZnO film. Under zero bias, these electrons are driven by the potential difference across the channel and collected at the two electrodes. Figure 7c discloses a performance degradation of 11.84% after sustaining 50 bending cycles. Nevertheless, the degradation is exaggerated between 50 and 100 bending cycles, as presented in Figure S7 (Supporting Information). To figure out the origin of this quality deterioration, we detected both ZnO and 2D α-C:H surfaces after 100 bending cycles by SEM. No visible cracking was observed. In addition, a pristine ZnO film was sputtered on the polyimide with the same parameters to carry out a repeated bending test. As shown in Figure S7 (Supporting Information), tremendous conductivity decreases by 19.16% and 43.22% are observed after

**ADVANCED
SCIENCE NEWS**
www.advancedsciencenews.com

**ADVANCED
OPTICAL
MATERIALS**
www.advopticalmat.de

Figure 7. a) *I–t* curves of the flexible ZnO/2D α-C photodetector subjected to zero bias, 0.45% tensile strain, and laser exposures of 365, 520, and 635 nm, respectively. b) Band alignment at the ZnO/2D α-C interface inducing the piezo-phototronic effect under the tensile strain. c) *I–t* curves showing the performance degradation after 50 bending cycles under the tensile strain and the 365 nm illumination. d) Figures of merit of the photodetectors under different testing conditions, namely, responsivity (*R*), external quantum efficiency (EQE), detectivity (*D**), and rise time (τ_{rise}).

50 and 100 bending cycles, respectively. Hence, we attribute the performance degradation of the ZnO/2D α-C:H photodetector to the poor mechanical durability of the polycrystalline ZnO film. This bending performance, although is comparable to some reported results,[3,46–49] requires further optimization. As a proof-of-concept demo, our device sheds light on the 2D α-C:H as an emerging candidate for self-powered flexible photodetectors.

For a better performance evaluation, we extract the key figures of merit of the photodetectors, namely, responsivity (*R*), external quantum efficiency (EQE), and detectivity (*D**). These properties are defined in the following expressions

$$R = I_{ph}/p \cdot A \tag{1}$$

$$EQE = I_{ph}/(A \cdot e)/(p/hv) \tag{2}$$

$$D^* = R \cdot A^{1/2}/(2eI_{dark})^{1/2} \tag{3}$$

where *A*, *p*, *h*, *e*, and *v* are the effective channel area, the power density of the laser incident on the device, the Planck constant, the elementary charge, and the frequency of the incident laser,

respectively. As indicated in Figure 7d, all above traits, along with τ_{rise}, experience remarkable optimization under the synergistic impact of the heterogeneous integration and tensile strain. Specifically, 24.28-fold *R* and EQE enhancement, as well as 65.89-fold *D** elevation are obtained. This gives the optimal self-powered performance of an *R* of 195.16 mA W^{-1}, an EQE of 66.29%, a *D** of 6.03×10^8 Jones, and a τ_{rise} of 20 ms, respectively. As enumerated in Table S1 (Supporting Information), our devices see an overall advancement compared to the state-of-the-art self-powered flexible photodetectors, especially the ZnO-based heterojunction ones. Further performance enhancement can be achieved by applying the external bias for more efficient carrier separation and migration, as shown in Figure S7 (Supporting Information).

3. Conclusion

We present a cost-effective synthesis of 2D α-C:H nanosheets of large-scale, ultrasmooth surface, high structural homogeneity, and long-term chemical stability. Comprehensive and self-consistent structural analyses unravel the nanosheets' layering feature, stacking by disordered sp^3 network embedded with crystalline sp^2 nanoclusters. The growth of the nanosheets follows the

typical "vapor–solid" mechanism fulfilling the thermodynamic requirement in the Berman–Simon phase diagram. The optical characterizations demonstrate the transmittance over 97.7% covering a broad range of 425–1300 nm, as well as the absorption and PL spectral overlap within 385–420 nm. Self-powered and flexible photodetectors based on the ZnO/2D α-C:H heterojunction are fabricated, mechanically durable of 50 bending cycles. Tremendous property advancements have been demonstrated, including extended photosensitive band, a responsivity of 195.16 mA W^{-1}, and a 267-fold τ_{rise} shortening. The performance optimization derives from the congruous impacts of the type II heterogeneous integration, the piezo-phototronic effect, and the pyroelectric effect. This emerging 2D allotropic form of carbon has established itself as an intriguing material for bidirectional optical signal transmission, optical communication, and next-generation transparent and flexible electronics and optoelectronics.

4. Experimental Section

Fabrication of 2D α-C Nanosheets: For the synthesis of pristine g-C$_3$N$_4$, 10 g of urea was dried at 80 °C for a day before covered by a lid and then transferred to the furnace. The heating was programed under a rate 2 °C min^{-1} and then kept at 550 °C for 3 h. After naturally cooling down to room temperature, the creamy yellow g-C$_3$N$_4$ powders shown in Figure 1a were collected for the next use.

For the synthesis of 2D nanosheets, 200 mg of the pristine g-C$_3$N$_4$ was transferred into a 25 cm quartz tube with an external diameter of 12 mm and a wall thickness of 1.5 mm. The quartz tube was vacuumed through a rubber tube with a water pump, and then immediately sealed by a high-temperature blaze gun at a position of 12 cm away from the tube end. The sealed tube containing pristine g-C$_3$N$_4$ was put into the furnace for calcination at 550 °C for 3 h. After the thermal treatment and natural cooling, the original yellow powders turned into milky colored ones, whereas nanosheets with white crystal shine were strongly stuck to the tube wall at the other end, as shown in Figure 1a. Immediately after the tube was broken, the nanosheets were dispersed in ethanol.

Chemical and Structural Characterization: The SEM Imaging was performed in Carl Zeiss MERLIN of Raith Pioneer Two at an extra high-tension (EHT) voltage of 5 kV and a working distance of 10 mm. The Bruker QUANTAX 200 detector was used to collect the EDS data. STEM images were acquired using a double-Cs-corrected Titan Cubed Themis G2 with the acceleration voltage being typically set to 80 kV. The EELS spectra were acquired in Quantum ER/965 P with a maximal resolution of 0.17 eV. The optical microscope images were taken from a SOPTOP RX50M optical microscope. XRD patterns were collected by Rigaku MiniFlex600 with Cu Kα radiation (λ = 1.5104 Å) operating at 45 kV and 200 mA. AFM images were acquired by scanning probe microscopy (SPM, AIST). The morphological observation and thickness extraction were done by the AIST software while the roughness measurement was done by the Gwyddion software. XPS measurements were performed in an ESCALAB 250XI (Thermo Scientific) equipped with a monochromatic Al Kα X-ray gun (1486.6 eV), a photoelectron spectrometer, and a hemispherical energy analyzer in an ultrahigh vacuum chamber (base pressure = 5–10 mbar). Samples were pretreated by etching with argon plasma for 30 s before measurement to remove the surface pollutants. The deconvolution of the detected peaks was done in the XPS peak 41 software. FTIR spectra were collected in a Thermo Scientific Nicolet iS50 FTIR spectrometer system at room temperature in the 400–4000 cm^{-1} wavenumber range. The Raman measurements were conducted in an iHR550 spectrometer, and the measuring grating was 300 lines mm^{-1}. A 100× immersion objective lens with a numerical aperture of 1.49 was used for both excitation and collection of the scattered light from the sample. The measurements were performed at room temperature under the excitation of 660 nm and the laser power (at the sample) less than 3 mW.

Optical and Optoelectrical Measurements: PL spectra were measured using a fluorescence spectrophotometer (HORIBA LabRAM HR Evolution) under the excitation of a 325 nm laser. UV–vis–NIR absorption spectra were obtained from a PerkinElmer LAMBDA spectrophotometer in 350–1650 nm wavelength range.

For the fabrication of flexible devices, the ZnO films were grown on the polyimide substrate by sputtering at 300 °C for 15 min at the pressure of 0.5 Pa. The electrodes were deposited by sputtering Ti (2 nm) and Au (50 nm), whereas the channel areas were defined by a home-designed patterned mask. The heterojunction was formed via dispersing the suspension containing 2D α-C nanosheets onto the pristine ZnO film and then naturally drying. The rigid devices were manufactured by procedures assembling to the flexible ones, where the commercial ZnO films on sapphire (001) substrates were utilized.

The photodetectors were characterized under the radiation of continuous wave (c.w.) lasers in the wavelength range of 365–635 nm. A calibrated power meter was used to measure the incident power at each wavelength. During the test, the lasers were positioned 1.5 cm above the photodetectors and focused onto the channels with the beam diameters of ≈1–6 mm. The I–V curves were measured by Keysight B2902A semiconductor analyzers under light exposure for 1 min, in order to obtain the steady current under light exposure. The I–t curves were obtained in the same facility by manually turning on and off the laser with periodic durations.

Supporting Information

Supporting Information is available from the Wiley Online Library or from the author.

Conflict of Interest

The authors declare no conflict of interest.

[1] S. Cai, X. Xu, W. Yang, J. Chen, X. Fang, *Adv. Mater.* **2019**, *31*, 1808138.

[2] T. L. Shen, Y. W. Chu, Y. K. Liao, W. Y. Lee, H. C. Kuo, T. Y. Lin, Y. F. Chen, *Adv. Opt. Mater.* **2020**, *8*, 1901334.

[3] V. M. Diep, A. M. Armani, *Nano Lett.* **2016**, *16*, 7389.

**ADVANCED
SCIENCE NEWS**

www.advancedsciencenews.com

**ADVANCED
OPTICAL
MATERIALS**

www.advopticalmat.de

[4] Y. J. Tan, H. Godaba, G. Chen, S. T. M. Tan, G. Wan, G. Li, P. M. Lee, Y. Cai, S. Li, R. F. Shepherd, J. S. Ho, B. C. K. Tee, *Nat. Mater.* **2020**, *19*, 182.

[5] J. Wang, H. Fang, X. Wang, X. Chen, W. Lu, W. Hu, *Small* **2017**, *13*, 1700894.

[6] F. H. L. Koppens, T. Mueller, P. Avouris, A. C. Ferrari, M. S. Vitiello, M. Polini, *Nat. Nanotechnol.* **2014**, *9*, 780.

[7] Y. R. Lim, W. Song, J. K. Han, Y. B. Lee, S. J. Kim, S. Myung, S. S. Lee, K. S. An, C. J. Choi, J. Lim, *Adv. Mater.* **2016**, *28*, 5025.

[8] Y. Yang, X. Yang, X. Zou, S. Wu, D. Wan, A. Cao, L. Liao, Q. Yuan, X. Duan, *Adv. Funct. Mater.* **2017**, *27*, 1604096.

[9] Q. Bao, K. P. Loh, *ACS Nano* **2012**, *6*, 3677.

[10] H. Li, Y.-J. Zeng, X. J. Hu, H. H. Zhang, S. C. Ruan, M. J. Van Bael, C. Van Haesendonck, *Carbon* **2017**, *124*, 193.

[11] F. Xia, H. Wang, J. C. M. Hwang, A. H. C. Neto, L. Yang, *Nat. Rev. Phys.* **2019**, *1*, 306.

[12] L. Hu, M. N. Amini, Y. Wu, Z. Jin, J. Yuan, R. Lin, J. Wu, Y. Dai, H. He, Y. Lu, J. Lu, Z. Ye, *Adv. Opt. Mater.* **2018**, *6*, 1800440.

[13] L. Hu, J. Yuan, Y. Ren, Y. Wang, J. Yang, Y. Zhou, Y. Zeng, *Adv. Mater.* **2018**, *30*, 1801232.

[14] Y. Noda, C. Merschjann, J. Tarábek, P. Amsalem, N. Koch, M. J. Bojdys, *Angew. Chem., Int. Ed.* **2019**, *58*, 9394.

[15] Z. Yang, H. Zhang, J. Xu, R. Ma, T. Sasaki, Y. Zeng, S. Ruan, H. Yanglong, *Natl. Sci. Rev.* **2020**, *7*, 841.

[16] B. R. Sharma, A. Manjanath, A. K. Singh, *Sci. Rep.* **2014**, *4*, 7164..

[17] B. Ram, H. Mizuseki, *Carbon* **2020**, *158*, 827.

[18] S. Kim, M. Ju, J. Lee, J. Hwang, J. Lee, *J. Am. Chem. Soc.* **2020**, *142*, 9250.

[19] J. Robertson, *Mater. Sci. Eng., R* **2002**, *37*, 129.

[20] Y.-J. Zeng, N. Gauquelin, D.-Y. Li, S.-C. Ruan, H.-P. He, R. Egoavil, Z.-Z. Ye, J. Verbeeck, J. Hadermann, M. J. Van Bael, C. Van Haesendonck, *ACS Appl. Mater. Interfaces* **2015**, *7*, 22166.

[21] A. C. Ferrari, J. Robertson, *Philos. Trans. R. Soc., A* **2004**, *362*, 2477.

[22] J. Müller, W. Ibach, K. Weishaupt, O. Hollricher, *Confocal Raman Microscopy*, 2nd ed., Springer, Berlin **2018**.

[23] P.-H. Tan, *Raman Spectroscopy of Two-Dimensional Materials*, Springer, Singapore **2019**.

[24] A. C. Ferrari, J. C. Meyer, V. Scardaci, C. Casiraghi, M. Lazzeri, F. Mauri, S. Piscanec, D. Jiang, K. S. Novoselov, S. Roth, A. K. Geim, *Phys. Rev. Lett.* **2006**, *97*, 187401.

[25] A. C. Ferrari, J. Robertson, *Phys. Rev. B: Condens. Matter Mater. Phys.* **2001**, *64*, 075414.

[26] A. C. Ferrari, J. Robertson, *Phys. Rev. B: Condens. Matter Mater. Phys.* **2000**, *61*, 14095.

[27] A. C. Ferrari, D. M. Basko, *Nat. Nanotechnol.* **2013**, *8*, 235.

[28] J. Schäfer, J. Ristein, R. Graupner, L. Ley, U. Stephan, T. Frauenheim, *Phys. Rev. B: Condens. Matter Mater. Phys.* **1996**, *53*, 7762.

[29] Z. L. Wang, *Mater. Sci. Eng., R* **2009**, *64*, 33.

[30] H. J. Fan, P. Werner, M. Zacharias, *Small* **2006**, *2*, 700.

[31] A. Pospischil, M. Humer, M. M. Furchi, D. Bachmann, R. Guider, T. Fromherz, T. Mueller, *Nat. Photonics* **2013**, *7*, 892.

[32] C. Bao, W. Xu, J. Yang, S. Bai, P. Teng, Y. Yang, J. Wang, N. Zhao, W. Zhang, W. Huang, F. Gao, *Nat. Electron.* **2020**, *3*, 156.

[33] C. Geng, Y. Jiang, Y. Yao, X. Meng, J. A. Zapien, C.-S. Lee, Y. Lifshitz, S. T. Lee, *Adv. Funct. Mater.* **2004**, *14*, 589.

[34] L. Hu, Q. Liao, Z. Xu, J. Yuan, Y. Ke, Y. Zhang, W. Zhang, G. P. Wang, S. Ruan, Y. J. Zeng, S. T. Han, *ACS Photonics* **2019**, *6*, 886.

[35] Y. J. Zeng, Z. Z. Ye, W. Z. Xu, D. Y. Li, J. G. Lu, L. P. Zhu, B. H. Zhao, *Appl. Phys. Lett.* **2006**, *88*, 062107.

[36] W. J. Ong, L. L. Tan, Y. H. Ng, S. T. Yong, S. P. Chai, *Chem. Rev.* **2016**, *116*, 7159.

[37] Y. Wang, L. Zhu, Y. Feng, Z. Wang, Z. L. Wang, *Adv. Funct. Mater.* **2019**, *29*, 1807111.

[38] Z. L. Wang, J. Song, *Science* **2006**, *312*, 242.

[39] Z. Xu, Y. Zhang, Z. Wang, *J. Phys. D: Appl. Phys.* **2019**, *52*, 223001.

[40] Y. Guo, Y. Song, Y. Mang, Z. Xu, H. Xie, H. Li, Z. Li, H. Liang, S. Ruan, Y.-J. Zeng, *J. Mater. Chem. C* **2020**, *8*, 13226.

[41] S. Yu, Q. Rice, B. Tabibi, Q. Li, F. J. Seo, *Nanoscale* **2018**, *10*, 12472.

[42] M. K. Mohanta, A. Rawat, N. Jena, Dimple, R. Ahammed, A. De Sarkar, *ACS Appl. Mater. Interfaces* **2020**, *12*, 3114..

[43] M. K. Mohanta, A. Rawat, Dimple, N. Jena, R. Ahammed, A. De Sarkar, *Nanoscale* **2019**, *11*, 21880.

[44] M. K. Mohanta, A. De Sarkar, *ACS Appl. Mater. Interfaces* **2020**, *12*, 18123.

[45] M. M. Yang, Z. D. Luo, Z. Mi, J. Zhao, S. P. E, M. Alexe, *Nature* **2020**, *584*, 377.

[46] H. Sun, W. Tian, F. Cao, J. Xiong, L. Li, *Adv. Mater.* **2018**, *30*, 1706986.

[47] J. Yao, G. Yang, *Small* **2018**, *14*, 1704524.

[48] G. Mohan Kumar, X. Fu, P. Ilanchezhiyan, S. U. Yuldashev, D. J. Lee, H. D. Cho, T. W. Kang, *ACS Appl. Mater. Interfaces* **2017**, *9*, 32142.

[49] R. Sinha, N. Roy, T. K. Mandal, *ACS Appl. Mater. Interfaces* **2020**, *12*, 33428.